



Article

Magnetic Properties and Microstructure of FePt(BN, X, C) (X = Ag, Re) Films

Jai-Lin Tsai ^{1,*} , Chun-Yu Sun ¹, Jhih-Hong Lin ¹, Yi-Yuan Huang ¹ and He-Ting Tsai ²¹ Department of Materials Science and Engineering, National Chung Hsing University, Taichung 402, Taiwan² Instrument Center, The Office of Research & Development, National Chung Hsing University, Taichung 402, Taiwan

* Correspondence: tsaijl@dragon.nchu.edu.tw; Tel.: +886-4-22840500 (ext. 308)

Abstract: A sputtered FePt(BN, Re, C) film, here boron nitride (BN), was compared to a reference sample FePt(BN, Ag, C). Intrinsically, these films illustrate a high anisotropy field (H_k) and perpendicular magnetocrystalline anisotropy (K_u), although the reference sample shows a higher value ($H_k = 69.5$ kOe, $K_u = 1.74 \times 10^7$ erg/cm³) than the FePt(BN, Re, C) film ($H_k = 66.9$ kOe, $K_u = 1.46 \times 10^7$ erg/cm³). However, the small difference in the anisotropy constant (K_2/K_1) ratio presents a close tendency in the angular dependence of the switching field. Extrinsically, the out-of-plane coercivity for the reference sample is 32 kOe, which is also higher than the FePt(BN, Re, C) film ($H_c = 27$ kOe), and both films present lower remanence ($M_{r(\text{parallel})}/M_{r(\text{perpendicular})} = 0.08\text{--}0.12$), that is, the index for perpendicular magnetic anisotropy. The higher perpendicular magnetization for both films was due to highly (001) textured FePt films, which was also evidenced by the tight rocking width of $4.1^\circ/3.0^\circ$ for (001)/(002) X-ray diffraction peaks, respectively, and high-enough ordering degree. The reference sample was measured to have a higher ordering degree ($S = 0.84$) than FePt(BN, Re, C) ($S = 0.63$). As a result, the Ag segregant shows stronger ability to promote the ordering of the FePt film; however, the FePt(BN, Re, C) film still has comparable magnetic properties without Ag doping. From the surface and elemental composition analysis, the metallic Re atoms found in the FePt lattice result in a strong spin–orbital coupling between transition metal Fe (3d electron) and heavy metals (Re, Pt) (5d electron) and we conducted high magnetocrystalline anisotropy (K_u). Above is the explanation that the lower-ordered FePt(BN, Re, C) film still has high-enough K_u and out-of-plane H_c . Regarding the microstructure, both the reference sample and FePt(BN, Re, C) show granular structure and columnar grains, and the respective average grain size and distributions are 6.60 nm (12.5%) and 11.2 nm (15.9%). The average widths of the grain boundaries and the aspect ratio of the columnar grain height are 2.05 nm, 1.00 nm, 2.35 nm, and 1.70 nm, respectively.

Keywords: out-of-plane coercivity; perpendicular magnetocrystalline anisotropy; spin–orbital coupling; columnar grains; granular structure



Citation: Tsai, J.-L.; Sun, C.-Y.; Lin, J.-H.; Huang, Y.-Y.; Tsai, H.-T. Magnetic Properties and Microstructure of FePt(BN, X, C) (X = Ag, Re) Films. *Nanomaterials* **2023**, *13*, 539. <https://doi.org/10.3390/nano13030539>

Academic Editor: Efrat Lifshitz

Received: 12 January 2023

Revised: 19 January 2023

Accepted: 21 January 2023

Published: 29 January 2023



Copyright: © 2023 by the authors. Licensee MDPI, Basel, Switzerland. This article is an open access article distributed under the terms and conditions of the Creative Commons Attribution (CC BY) license (<https://creativecommons.org/licenses/by/4.0/>).

1. Introduction

Energy-assisted magnetic recording is an alternative way to overcome the trilemma effect (superparamagnetic effect of CoCrPt oxides) in conventional perpendicular magnetic recording (PMR) and heat-assisted magnetic recording (HAMR) with L10 FePt media is the mainstream technology to target the hard disk area density beyond 4 Tb/in² in the near future. The L10 FePt film, which has higher magnetocrystalline anisotropy (K_u), is the optimal media in the HAMR system [1–4] and the hard disk drive (HDD) based on FePt media is currently being tested on data center customers [5–8].

To apply FePt media to HAMR, many works have discussed this extensively for decades. For HAMR media, perpendicular magnetic anisotropy (PMA) of the FePt film was a key requirement to extend the area density to ultrahigh and increase the capacity in HDD [1–4]. After annealing the disordered face-centered cubic FePt alloy with nearly

equal atomic compositional range, the ordered L10 phase with face-centered tetragonal (fct) structure, which has high K_u [1–4], was formed. As a result, magnetron sputtering and high-temperature deposition became the main technologies to prepare ordered L10 FePt films with high K_u . Many elements, for example, silver (Ag), copper (Cu), etc., have been doped to lower the L10 FePt ordering temperature and Curie temperature, which influenced the process deposition temperature and the laser writing (heat) power during thin-film engineering [9–11]. In addition, the structure requirement for perpendicular magnetic anisotropy tuned the surface energy and lattice misfit strain between the FePt and MgO-based underlayer [12–16] and CrRu seed layers [14,17,18], and sputtered the FePt film with (00L) orientation. In addition, to obtain a uniform granular structure and columnar grains to avoid noise and increase the signal-to-noise ratio, multiple segregants are required and Ag, carbon (C), and boron nitride (BN) are typical grain boundary materials for perpendicular FePt media [5,6,19]. The C has strong phase separation and diffusive ability to separate FePt grains and will initiate lateral growth and interrupt the columnar grains when the C concentration is much higher than the solubility. The amorphous BN was hard enough to support the FePt grains' growth upward in the columnar morphology. The Ag was used to enhance the FePt ordering via diffusion of Ag, which induces atom replacement through vacancies [5,6,9,19,20]. To study the FePt-X composite films, interface chemistry in heterostructures [21] and other functional alloy, oxide and composite films prepared in sputtering [22,23] and other thin-film formation technologies [24,25] was also addressed.

Multiple segregants are required in heat-assisted perpendicular magnetic recording media and BN, Ag, and C are necessary materials to co-sputter with the FePt layer and form a typical microstructure, which shows granular structure and columnar grains. In this work, the Ag segregant was replaced by the 5d element rhenium (Re). According to the reference report, 5d elements have large spin–orbital coupling that will influence the magnetocrystalline anisotropy of 3d metals; for example, in the order/disorder FePt alloy, the 5d element significantly enhanced the magnetocrystalline anisotropy through spin–orbital coupling and 3d–5d hybridization [26,27]. Based on this argument, different Re 5d elements were doped in the FePt system to form an FePt(Re) alloy film, and the grain boundary materials were parts of BN and C. Originally, the Ag was added to improve the FePt ordering degree, which is proportional to the magnetic anisotropy, and we then tried to break this relationship by preparing FePt(BN, Re, C), which has a lower ordering degree but comparable K_u . The achievement of this work is adding Re to replace the Ag segregant in the reference sample and that the FePt(BN, Re, C) film presents comparative magnetic properties and microstructures.

Furthermore, the magnetic media noise was reduced by reducing the intrinsic- and extrinsic parts of the switching field distribution (SFD) [2,3,27,28] and the SFD of two samples was measured. The major and minor magnetic hysteresis loops were measured to define and understand the magnetic characteristics, for example, dispersed magnetic H_k , misaligned c-axis, non-uniform grain size in extrinsic parts [26,27], and the grains' long-term dipole and short-term exchange coupling from extrinsic contribution [2,3].

2. Materials and Methods

The FePt(BN, Ag, C) and FePt(BN, Re, C) films were deposited by direct current magnetron sputtering on MgO (100) single-crystal substrate. The sputtering deposition equipment was designed to have main and pre-chambers and the substrate was moved via the load-lock feedthrough to the substrate holder, which has a heating system formed of a halogen lamp (OSRAM, 1000W) and cathodes (AJA, A320, North Scituate, MA, USA) set up in the main chamber. The two-inch-diameter composite targets FePt(BN, Ag, C) and FePt(BN, Re, C) were used. In order to compare the elemental Ag and Re doping effects precisely, the MgO (100) single crystal was used to provide the optimal baseline for the epitaxial growth of (001) textured FePt film. The MgO (100) substrate (HF-Kejing, 10 mm × 10 mm × 0.5 mm) was heated at 470 °C (the substrate surface temperature) for dry cleaning and then the magnetic layers with thickness of 15 nm were sputtered under an

Argon working pressure of 10 mTorr at 470 °C by the composite targets. The deposition rate of FePt(BN, Ag, C) (15 nm) and FePt(BN, Re, C) (15 nm) was 0.0372 nm/s and 0.0421 nm/s, respectively. In this study, the FePt(BN, Ag, C) was named as the reference sample because of the typical segregants (BN, Ag, C) used in HAMR media.

The crystal structure was measured using standard X-ray diffraction (XRD) (BRUKER, D8 Discover). The magnetization curves with in-plane and out-of-plane measured hysteresis loops were performed with a superconducting quantum interference device (SQUID) magnetometer (MPMS-XL). The sample microstructure was observed using transmission electron microscopy (TEM, JEOL JEM-2010). The surface analysis was measured using X-ray photoelectron spectroscopy (XPS, ULVAC-PHI 5000).

3. Results and Discussion

Figure 1 shows XRD patterns of (a) FePt(BN, Ag, C) (reference sample) and (b) FePt(BN, Re, C) films. Based on the crystal structure, the strong (001) and weak (003) superlattice peaks were present because of the ordered L1₀ FePt phase (JCPDS 43-1359) and the (002) fundamental reflection peak was also indexed (fcc FePt, JCPDS card no. 00-029-0718). The lattice constant “c” was calculated using the (001) diffraction peaks and the values are 0.3728 nm and 0.3743 nm, respectively. In addition, the (110) diffraction peak was measured using grazing incident diffraction (GID) that is similar to the in-plane XRD and the lattice constant “a” that was estimated with values of 0.3889 nm and 0.3857. The reference sample presents a smaller c/a ratio (0.959), which means higher ordering (more tensile stress on axis “a” and compressive force on axis “c”) as compared to the FePt(BN, Re, C) film with c/a = 0.970. Another way to estimate the FePt ordering degree is by using B. E. Warren’s equation [29,30]; the ordering degree is $(I_{(001)}/I_{(002)})^{1/2}/(I_{(002)}^*/I_{(001)}^*)^{1/2}$ and the values are 0.84 and 0.63, respectively. The $(I_{(002)}^*/I_{(001)}^*)^{1/2}$ value was calculated using film thickness and the width of half intensity in rocking curve, in theory [29,30], and $I_{(001)}I_{(002)}$ is the peak’s integrated intensity ratio for textured (001) FePt films and the respective values are 2.04 and 1.15 in (a) and (b). In Figure 1b, there is the fct/fcc structured FePt (200) tiny peak, indexed at 47.0°, which contributes to the c-axis misalignment and lowers the ordering degree of the FePt(BN, Re, C) film. The c-axis misalignment mentioned above can be measured using the rocking curves and width at a half intensity of FePt (001)/(002); the peaks are 4.09°/3.03° and 4.09°/3.07° in Figure 1c,d. The (002) rocking curve was asymmetric due to the overlap of (200) and (002) peaks and a little wider in the FePt(BN, Re, C) sample. In summary, the reference sample and FePt(BN, Re, C) film were hetero-epitaxially grown on MgO(100) and have a strong (001) texture.

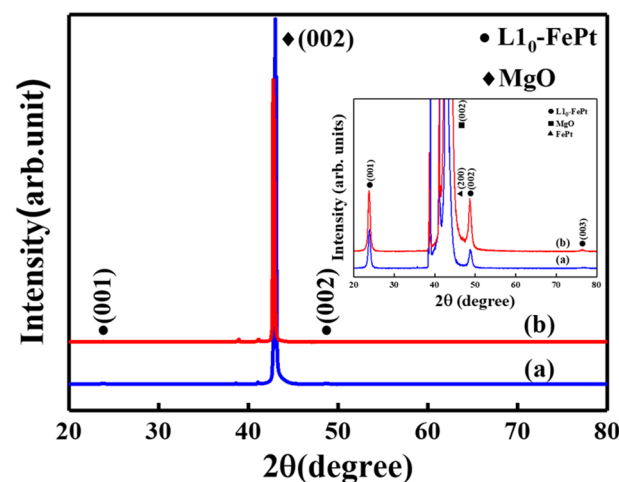


Figure 1. Cont.

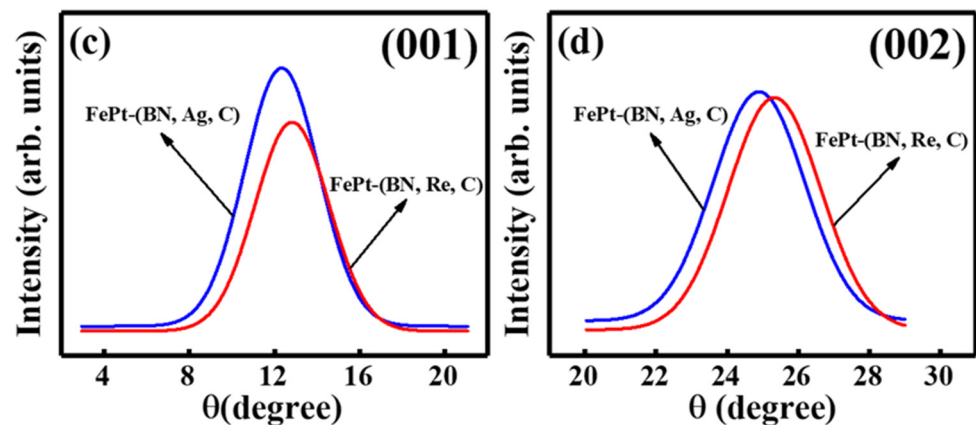


Figure 1. XRD patterns of (a) reference sample, FePt(BN, Ag, C), and (b) FePt(BN, Re, C) film. In the inset picture, the MgO (100) single-crystal peak was trimmed from top to observe the ordered L1₀ FePt (00L) diffraction peaks. FePt(001)/(002) rocking curves of (c) FePt(BN, Ag, C) and (d) FePt(BN, Re, C) films (the fcc FePt [JCPDS card no. 00-029-0718], the tetragonal (ordered L1₀ FePt [JCPDS 43-1359])).

The perpendicular H_k magnetic anisotropy of the reference sample and FePt(BN, Re, C) film was proved by the in-plane and out-of-plane magnetic hysteresis loop measurements. The easy magnetization curve (out-of-plane) shows full and huge hysteresis and the hard direction is a linear-like curve with small loop areas in Figure 2. The out-of-plane coercivity (H_c) is 32 kOe, 27 kOe, and the (M_{r(in-plane)})/M_{r(out-of-plane)} ratio, which qualifies the perpendicular anisotropy as 0.12, 0.08, and the negative nucleation field, which is defined at 0.95 Ms, is −2.5 kOe and −1.8 kOe, respectively. In Table 1, the reference sample illustrates a higher magnetic anisotropic field (H_k), which equals to 2K_u/M_s (H_k = 69.5 kOe), magneto-crystalline anisotropy (K_u = 1.74 × 10⁷ erg/cm³) and saturation of magnetization (M_s = 502 kG), than the FePt(BN, Re, C) film intrinsically. The magnetic anisotropy field H_k was defined as the intersection point of easy- and hard-axes magnetic hysteresis loops. The reference sample FePt(BN, Ag, C) film shows a higher ordering degree (S) and also has higher magnetic anisotropy (K_u) than the FePt(BN, Re, C) film. Only 63% of the FePt(BN, Re, C) grains are ordered but this film still has high-enough K_u and H_c. For reference, the 5% concentration Co-Re shows higher K_u than Co-Pt [26]. It is suggested that Fe-Re also contributes to extra K_u magnetic anisotropy due to the higher spin-orbital coupling of heavy metal Re and hybridization with 3d Fe electrons. As a result, the high magnetic anisotropy (K_u and out-of-plane H_c) were proved in the relative lower ordered (S = 0.63) FePt(BN, Re, C) film without Ag segregation.

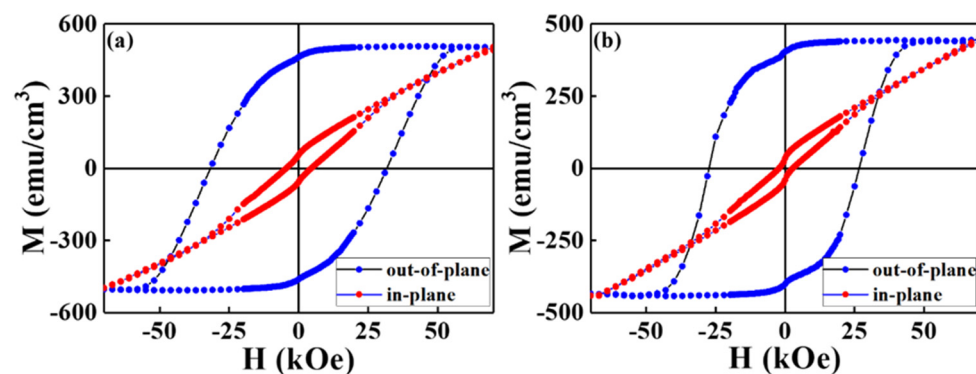


Figure 2. Room-temperature magnetic hysteresis loops of (a) reference sample, FePt(BN, Ag, C), and (b) FePt(BN, Re, C) films measured in easy (out-of-plane to film surface)- and hard (in-plane to film surface)-axis directions.

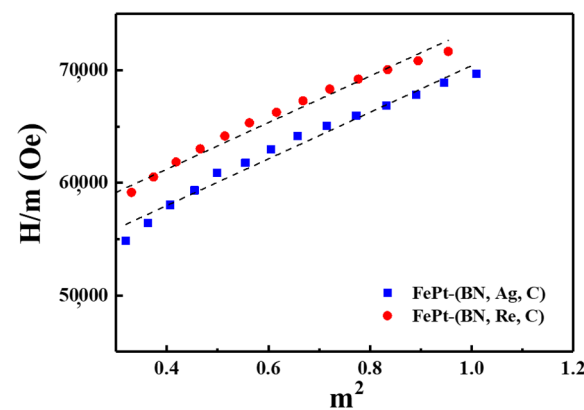
Table 1. Magnetic properties of reference FePt(BN, Ag, C) sample and FePt(BN, Re, C) films.

Sample	$H_{c\perp}$ (kOe)	$H_{c\parallel}$ (kOe)	M_s (T)	$M_{r\parallel}/M_{r\perp}$ (—)	K_u (erg/cm ³)	H_k (kOe)	H_N (kOe)
FePt(BN, Ag, C)	32	4.5	0.63	0.12	1.74×10^7	69.5	−2.5
FePt(BN, Re, C)	27	2.5	0.55	0.08	1.46×10^7	66.9	−1.8

From Table 1, the respective anisotropy fields (H_k) of the reference FePt(BN, Ag, C) and FePt(BN, Re, C) films are 69.5 and 66.9 kOe, and it is noteworthy that the values of K_u were often estimated from the slopes on the magnetization curves measured using a maximum applied field lower than the magnetic anisotropy H_k of L10-FePt, which was likely to result in certain errors in the estimation of K_u and which might confuse the discussion. Figure 3 illustrates the individual linear part in hard-axis curves for the reference sample, and the FePt(BN, Re, C) film and the K_1 and a high-order anisotropy constant K_2 were estimated using the following equation, respectively, [31,32]

$$\frac{H}{m} = \frac{2K'_1}{\mu_0 M_s} + \frac{4K_2}{\mu_0 M_s} m^2 \quad (1)$$

where $m = M/M_s$ is the normalized magnetization and K'_1 is the second-order anisotropy constant (Sucksmith–Thompson method). From the H/m versus m^2 plot, the K_1 and K_2 constants were conducted by the interception and the slope of the fitting curve [31,32]. The K_1 values are closer for the reference sample ($K_1 = 1.18 \times 10^7$ erg/cm³) and FePt(BN, Re, C) ($K_1 = 1.16 \times 10^7$ erg/cm³) after fitting with the Sucksmith–Thompson method and the K_2 values are 3.06×10^6 and 2.59×10^6 erg/cm³, respectively. The K_2/K_1 ratios of reference and FePt(BN, Re, C) samples were 0.26 and 0.22 and the small change in the anisotropy constant ratio means a close tendency in the angular dependence of the switching field.

**Figure 3.** Analysis of the hard-axis magnetization curve based on Sucksmith–Thompson method for reference FePt(BN, Ag, C) and FePt(BN, Re, C) films measured at room temperature.

The (dynamic) ordering temperature, degree, and magnetic anisotropic K_u constant were influenced by the FePt chemical composition, which was fixed to avoid any misleading. The MgO (100) single-crystal substrate was used and it is suggested that the structure variant of the FePt film was due to the slight dissolution of segregants at a high deposition temperature. The quite different ordering degree in the reference sample ($S = 0.84$) and FePt (Re, C, BN) film ($S = 0.63$) was because of the structure variant that also influenced the magnetic anisotropy K_u . Based on the reference reports [31,32], the K_{u1} and K_{u2} are proportional and independent to the ordering degree (S), respectively. In this study, the values of the ordering degree and magnetic anisotropic constant were a direct response to the Ag and Re segregants because the concentration of C and BN doping was the same in both samples. Adding the Ag element truly promotes the ordering degree and has higher

magnetic anisotropic constant (K_u). In the Sucksmith–Thompson method, the K_1 , which determines the switching behavior, has close values for two samples ($dK_1 \sim 0.02$) and the K_2 , which dominates the thermal stability, has large differences ($dK_2 \sim 0.47$). The K_1 is proportional to the ordering degree but the FePt(Re, C, BN) film presents extra spin–orbital coupling between Fe and Pt(Re), which enhances the K_1 value. As a result, the FePt(BN, Re, C) film shows a lower K_2/K_1 value ($0.22 < 0.26$).

Figure 4 presents the major and minor (recoil in variant field) magnetization loops to study the relationships between the magnetic switching behavior and grains' morphology, and the intrinsic and extrinsic switching field distribution was analyzed. When the loops recoiled in the coercivity field, half of the grains (50%) were switched in the easy axial direction and the parameters ΔH_{int} and ΔH_{ext} were collected after comparison with the major magnetic hysteresis curves. For reference FePt(BN, Ag, C) and FePt(BN, Re, C) films, the intrinsic ($\Delta H_{\text{int}} = 15.5$ kOe, 9.30 kOe) and extrinsic ($\Delta H_{\text{ext}} = 3.54$ kOe, 3.06 kOe) switching field distributions were determined in Figure 4a,b, respectively.

The intrinsic switching field distribution comes from grain-size distribution (σ_{volume}), magnetic anisotropy field dispersion (σ_{Hk}), and misalignment of the c -axis (σ_{axis}), and the extrinsic SFD comes from the grains' dipolar and exchange coupling [2,3,27,28]. The standard deviation (σ_{int}) of intrinsic SFD is estimated from the $\Delta H_{\text{int}}/1.35$ [2,3,27,28], and the $(\sigma_{\text{int}})^2$ can be written as the summary of $(\sigma_{\text{volume}})^2 + (\sigma_{\text{axis}})^2 + (\sigma_{\text{Hk}})^2$, because of the close values in rocking width ($\Delta\theta_{50}$) and average grain size in both samples; the grain-size distribution (σ_{volume}) and misalignment of the c -axis (σ_{axis}) terms were dropped. As a result, the SFD can be evaluated by the magnetic anisotropy field dispersion (σ_{Hk}) and the FePt (BN, Re, C) film illustrates smaller values. The small difference in extrinsic SFD (ΔH_{ext}) means that the equal grain decoupling in granular structure for two samples and the long-range magnetostatic coupling and inter-granular coupling were not considered in this study.

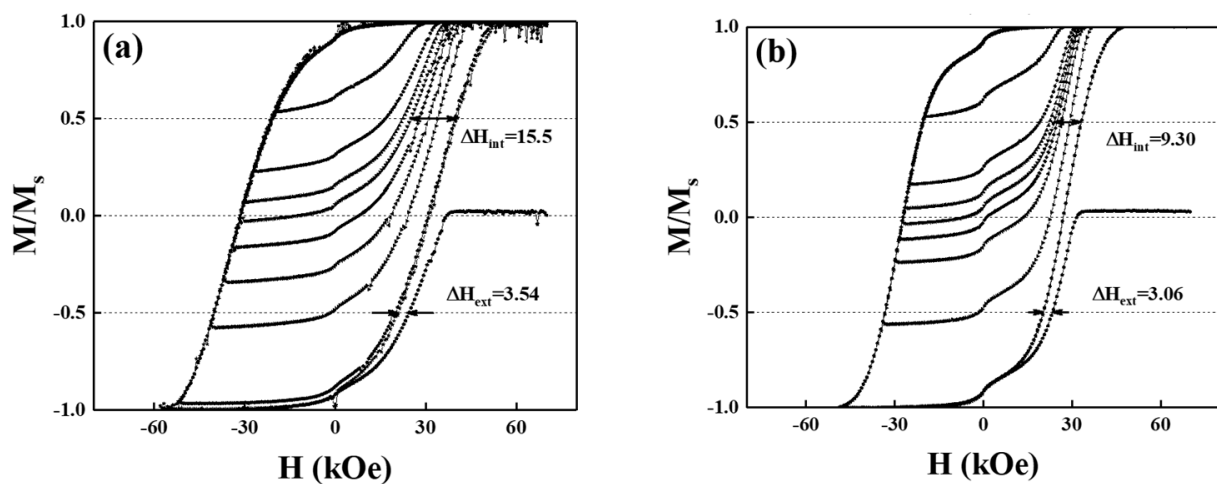


Figure 4. Major and minor loops of (a) reference FePt(BN, Ag, C) film and (b) FePt(BN, Re, C) film. The minor loop is used to measure intrinsic and extrinsic switching field distribution (SFD).

Figures 5 and 6 present the XPS of FePt(BN, Ag, C) and FePt(BN, Re, C) films. In Figure 5, in spite of metallic Fe, Pt, C, and Ag peaks, ferrite Fe_3O_4 and Fe satellite peak (Sat.) were also detected from the film surface after peak resolution. From the spectra line shape shown in Figures 5 and 6a, there are distinctive shoulders at the binding energy around 710 eV and 720 eV, and the Fe 2p_{3/2} and 2p_{1/2} core-level binding energy was considered and the Fe_3O_4 phase was observed both in FePt(BN, Ag, C) and FePt(BN, Re, C) films. The magnetite Fe_3O_4 (ferrimagnet) is a soft magnetic material and responds to the slight kink illustrated in the out-of-plane magnetization curves at zero field in Figure 2a [33,34].

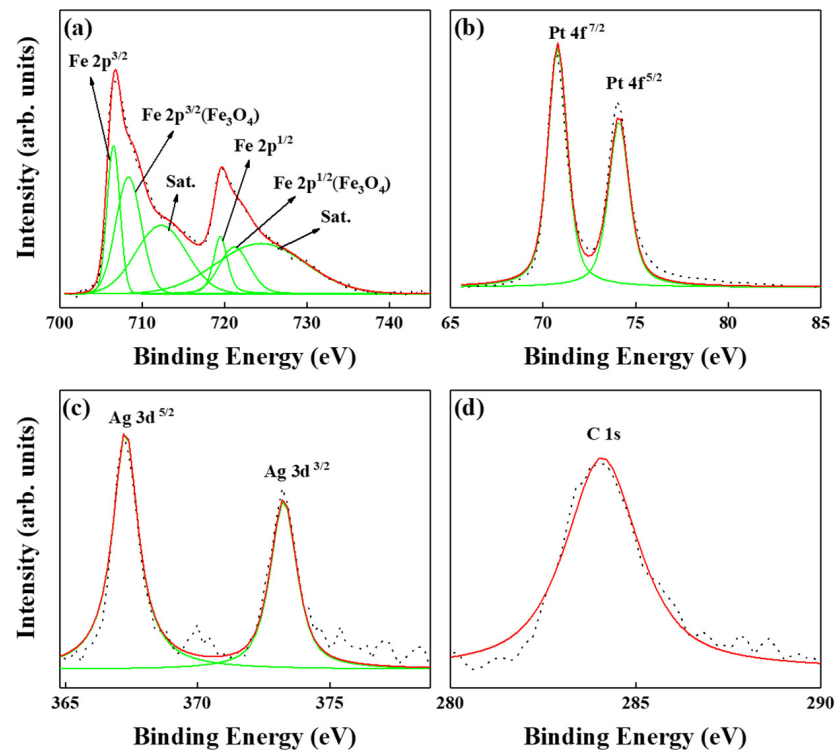


Figure 5. XPS of reference FePt(BN, Ag, C) film, (a) the metallic Fe, iron oxide was indexed, (b) Pt, (c) Ag, and (d) C.

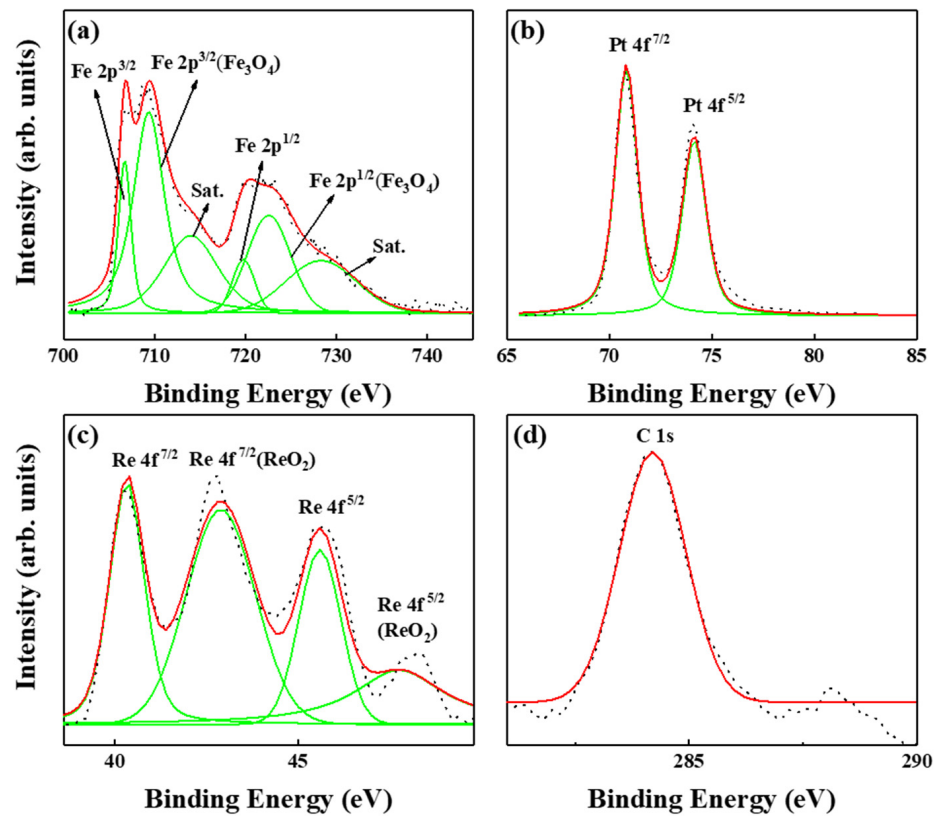


Figure 6. XPS of FePt(BN, Re, C) film, (a) metallic Fe, iron oxide were indexed, and (b) Pt, (c) metallic Re, and ReO₂ were indexed and (d) C.

The ferrite Fe_3O_4 was also observed in the XPS of the $\text{FePt}(\text{BN}, \text{Re}, \text{C})$ film in Figure 6a and the kink in the magnetization curve was more clear in Figure 2b. For inverse spinel ferrite Fe_3O_4 , the Fe^{3+} ions are divided into tetrahedral (A) and octahedral (B) sites equally and the Fe^{2+} ions are in B sites. In Figures 5 and 6, the $\text{Fe}^{2+}/\text{Fe}^{3+}$ ratio is higher in the $\text{FePt}(\text{BN}, \text{Re}, \text{C})$ film, which means that larger soft-magnetic moments contributed to the surface of the hard magnetic layer and a clear kink was observed in the hysteresis loops, as evidenced in Figure 2b [35–37]. In addition, the metallic Re, and ReO_2 appeared after considering the Re $4f^{5/2}$ and $4f^{7/2}$ core-level binding energy in Figure 6c. According to reference [38], the ReO_2 is dark blue or black in color and the crystal structure is in the monoclinic form below, 300°C , and orthorhombic between 300 and 1500°C . The $\text{FePt}(\text{BN}, \text{Ag}, \text{C})$ and $\text{FePt}(\text{BN}, \text{Re}, \text{C})$ thin-film surface oxidations were both indexed in XPS and the oxides were soft-magnetic Fe_3O_4 and ReO_2 , which may cause the lower ordering degree in the $\text{FePt}(\text{BN}, \text{Re}, \text{C})$ film due to the deviation in near-equal atomic FePt . Actually, the soft ferrite Fe_3O_4 causes the kink in magnetic hysteresis loops shown in Figure 2a,b and needs to be avoided in practical applications.

From the plane-view TEM images, the $\text{FePt}(\text{BN}, \text{Ag}, \text{C})$ and $\text{FePt}(\text{BN}, \text{Re}, \text{C})$ films show a typical uniform granular structure in which the FePt grains were separated by the segregants (Figure 7). In Figure 8a,b, the FePt grains are mono-distributed with average grain sizes $\langle D \rangle$ of 6.60 nm and 11.2 nm , and the grain-size distributions, defined by $(\sigma/\langle D \rangle)$, are 12.6% and 16.0% in the reference sample and $\text{FePt}(\text{BN}, \text{Re}, \text{C})$ film, respectively. The reference sample shows smaller and more uniform grains than the $\text{FePt}(\text{BN}, \text{Re}, \text{C})$ film and reflects the higher nucleation field (H_N) that was defined at the field of 0.95 Ms and out-of-plane coercivity (H_c), as presented in Table 1. However, the grains' density in the $\text{FePt}(\text{BN}, \text{Re}, \text{C})$ film was higher than in the reference sample because of the smaller grain boundaries' width ($1.00\text{ nm} < 2.05\text{ nm}$), which was estimated by the subtraction of $\langle D_c \rangle$ (centre-to-centre average grain size) to $\langle D \rangle$ (average grain size).

The coherence between FePt and $\text{MgO}(100)$ was confirmed by the orientation and periodicity of the bright-field Moire fringes caused by the interference of diffraction spot patterns between FePt and MgO and the periodicity (λ) is given by Equation (2) [39]

$$\lambda = \frac{1}{|\Delta g|} = \frac{d_{\text{FePt}}d_{\text{MgO}}}{\sqrt{d_{\text{FePt}}^2 + d_{\text{MgO}}^2 - 2d_{\text{FePt}}d_{\text{MgO}}\cos\alpha}} \quad (2)$$

where α is the relative angle between $\text{FePt}(001)$ and $\text{MgO}(002)$, and d_{FePt} and d_{MgO} are spacing between planes, Δg vector is reciprocal vectors between g_{FePt} and g_{MgO} [39].

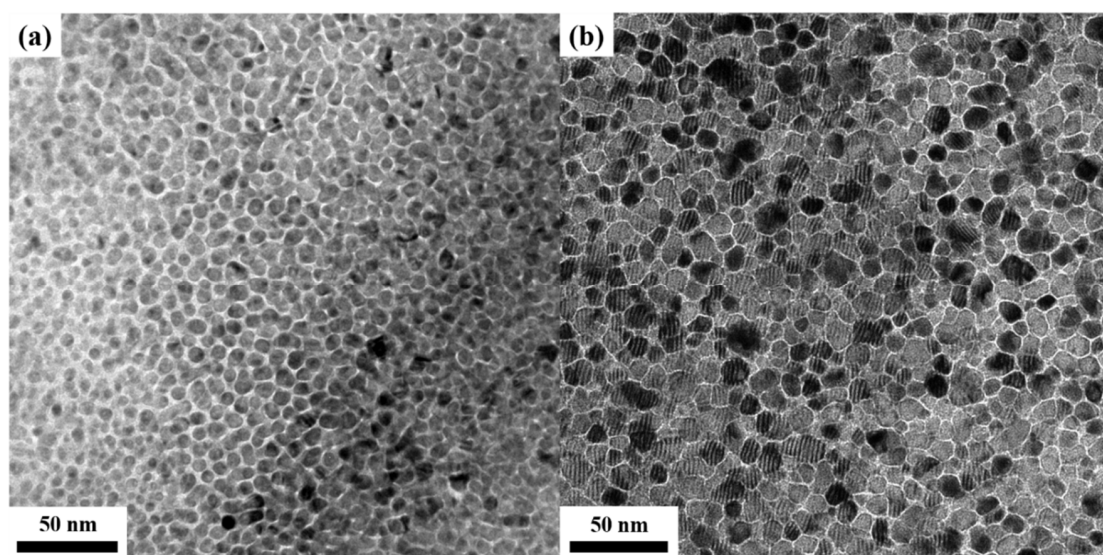


Figure 7. Cont.

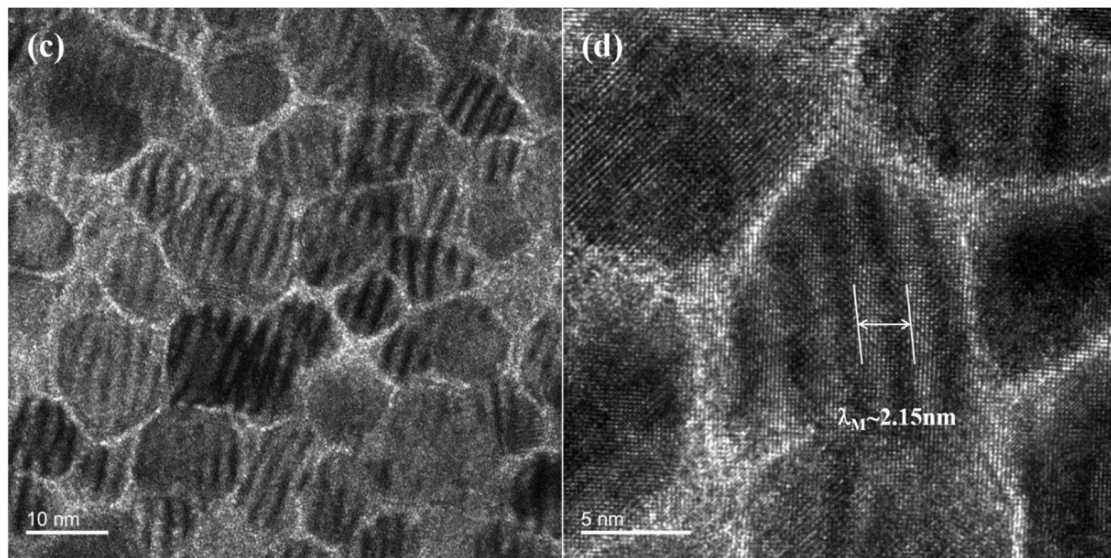


Figure 7. Plane-view TEM images of (a) FePt(BN, Ag, C) and (b) FePt(BN, Re, C) films; (c) Moire fringes in FePt(BN, Re, C) film and (d) selected grain to estimate the periodicity of Moire fringe.

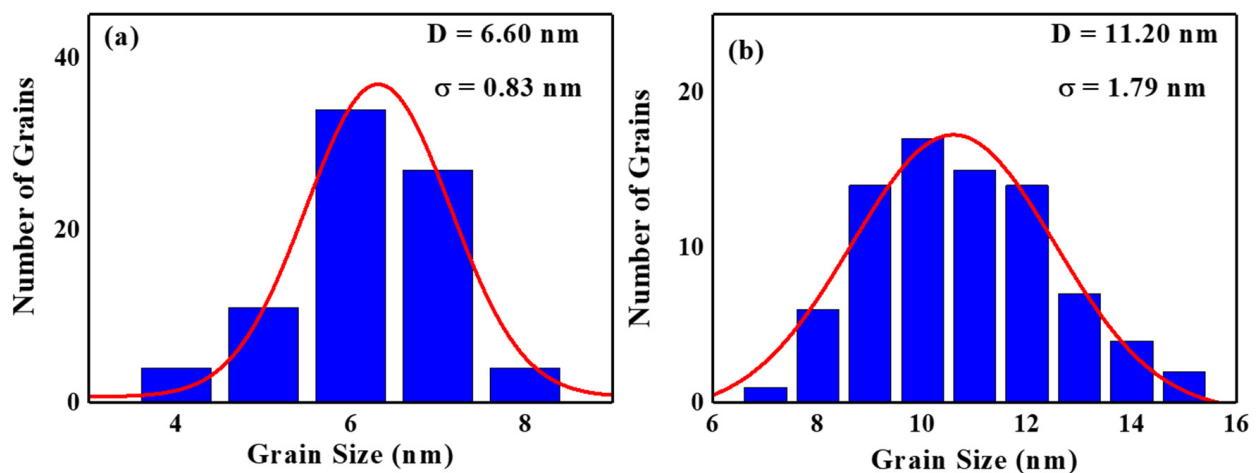


Figure 8. Average grain-size distribution $\langle D \rangle$ and standard deviation (σ) of (a) reference FePt(BN, Ag, C) sample and (b) FePt(BN, Re, C) films.

The mixed Moire fringe patterns can be observed in Figure 7c and the average periodicity is 2.33 nm (63.5°); for example, the individual period pattern is 2.15 nm, as measured in Figure 7d. When the epitaxial coherency is perfect, the alpha value is 0 but the rotational angle between FePt(001) and MgO(002) in this work is around 63.5° , calculated by Equation (1), which means non-perfect epitaxial growth in the FePt(BN, Re, C)/MgO system.

For the light atoms, for example, B, C, and N elements we chose to detect them via electron energy loss spectroscopy (EELS) with beam sizes smaller than 5 nm; the EELS spectrum of FePt(BN, Re, C) is shown in Figure 9. The B element was observed both in FePt lattice and grain boundaries and the C and N elements were segregated in the grain boundaries. After overlapping, part of the BN and C was found clearly in the grain boundaries. The unexpected O element, which may come from the natural oxidation during high-temperature deposition, was also observed at the grain's boundary and the surface oxides, for example, ReO_x and Fe_3O_4 were indexed in the XPS.

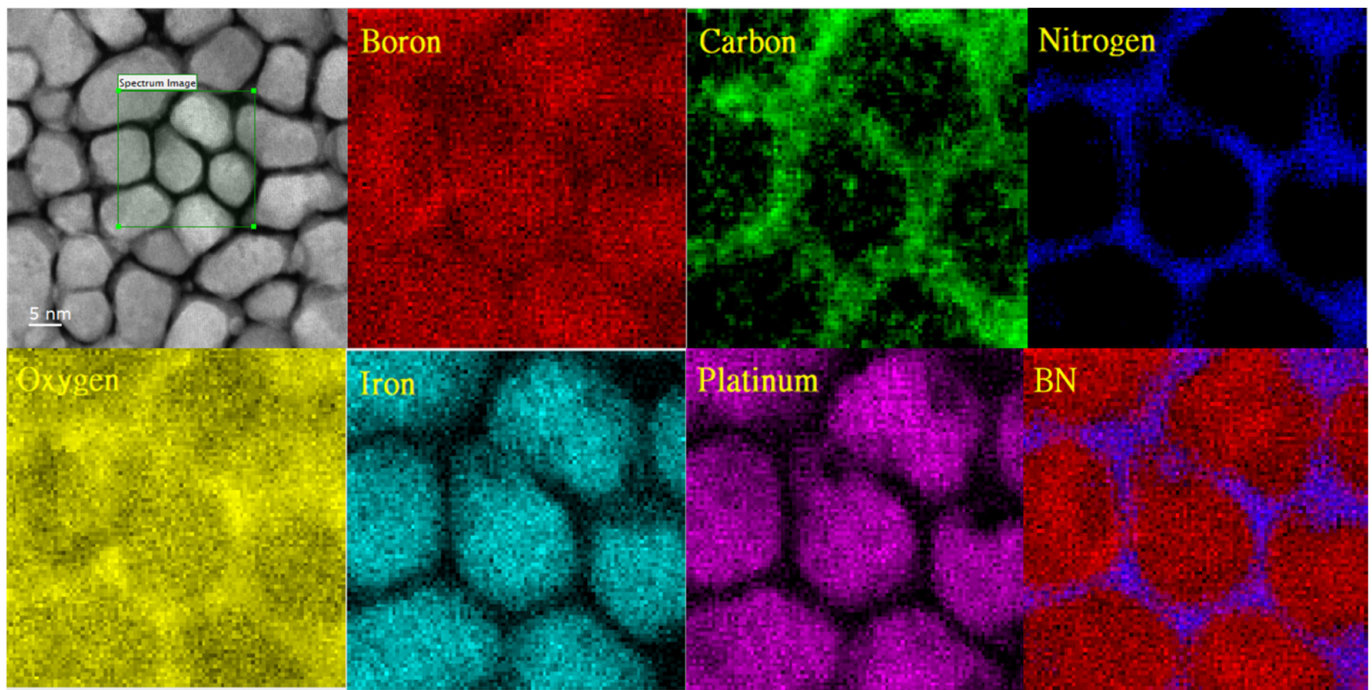


Figure 9. EELS mapping of Fe, Pt, B, N, C, and O elements by HRTEM for FePt(BN, Re, C) film.

The columnar grain structure was observed both in the reference sample and FePt(BN, Re, C) film in Figure 10a,b and the average aspect ratio of grains was defined from the film thickness to grain width (t/w), where the values are 2.35 and 1.70, respectively. Some columnar grains were interrupted and non-uniform due to the thicker FePt film (15 nm), but the highest-aspect-ratio FePt grains were demonstrated in this study. The insets show that the nanobeam diffraction patterns and the $\{0KL\}$ planes were indexed.

To provide more evidence of the element distribution, energy-dispersive X-ray (EDX) mapping was performed to analyze the composition in the reference sample and FePt(BN, Re, C) film. The cross-sectional high-angle angular dark-field (HAADF) images are shown in Figures 11 and 12. Both Fe and Pt elements are presented almost in the same position and grain areas and most of the Ag element were distributed in the FePt columnar grains' edges, as shown in Figure 11. Because the Ag atoms were rejected or diffused out at a high deposition temperature and occupied the Fe sites that decreased the coordination number, a Ag shell was formed [1,40]. The signal of B and C elements was not observed in EDX mapping but proved in the EELS image. The N element was distributed thoroughly in FePt grains and boundary areas in EDX mapping in Figures 11 and 12 but more segregated at the grain boundaries in EELS mapping presented in Figure 9. In principle, the EELS mapping data are more accurate for light element N. In Figure 12, the heavy metallic Re appeared in the FePt grains and was accumulated at the FePt(BN, Re, C) and MgO interface, and the Re was overlapped with O and formed ReO_2 on the FePt grain surface. It is suggested that the metallic Re will replace part of the Fe in the FePt lattice due to the formation of iron oxide on the film surface and the composition was shifted a little to the Pt-rich FePt(Re) alloy. Furthermore, the hybridization of 3d Fe and 5d Pt(Re) electrons presents high spin-orbital coupling, which reflects high magnetocrystalline anisotropy (K_u).

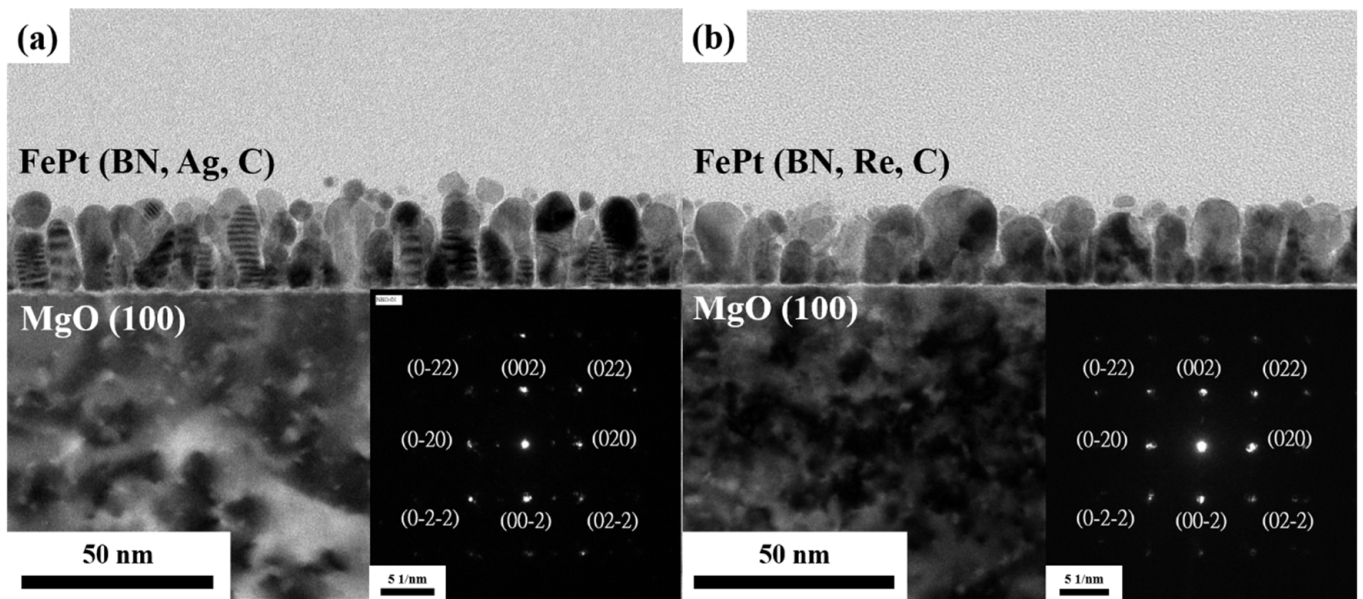


Figure 10. Cross-section TEM images of (a) FePt(BN, Ag, C) and (b) FePt(BN, Re, C) films. Insets are nanobeam diffraction patterns.

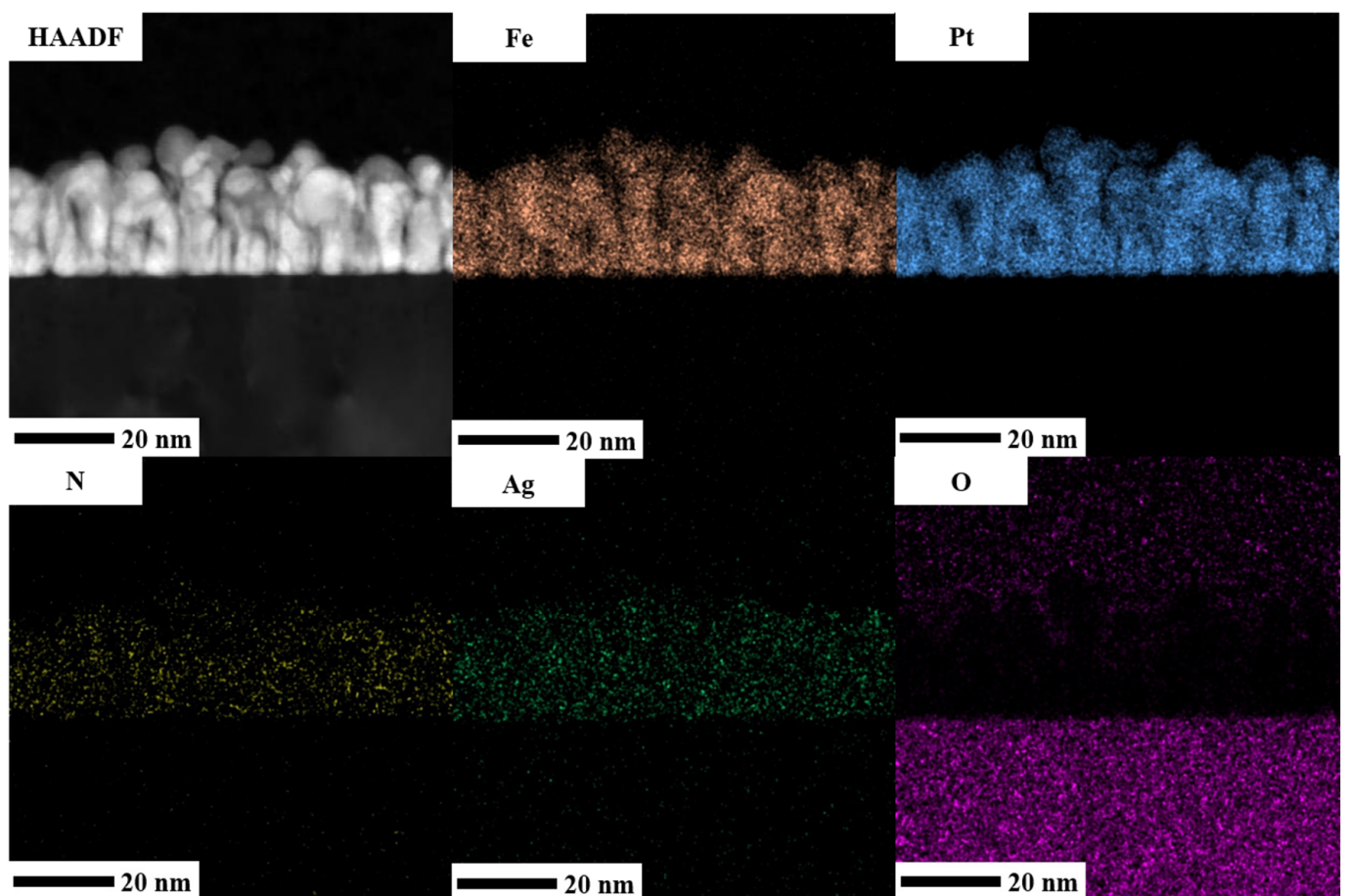


Figure 11. High-angle angular dark-field (HAADF) image and EDX mapping of Fe, Pt, Ag, N, and O elements of FePt(BN, Ag, C) film.

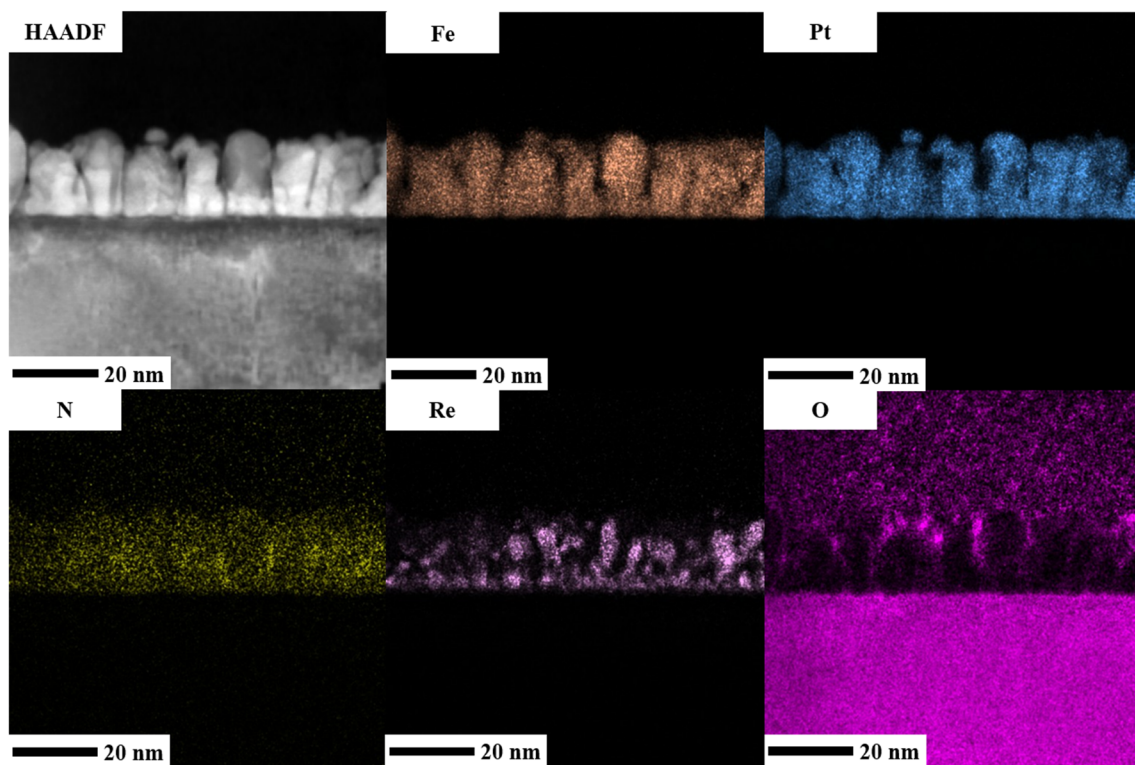


Figure 12. High-angle angular dark-field (HAADF) image and EDX mapping of Fe, Pt, N, and O elements of FePt(BN, Re, C) film.

4. Conclusions

In conclusion, the Re segregant in the FePt film did not improve the ordering degree like Ag but induced extra Fe-Pt(Re) spin–orbital coupling. As a result, the magnetic anisotropic field H_k and K_u can still be high as compared to the reference sample FePt(BN, Ag, C). It is suggested that 5d heavy transition metal segregants such as Re may compensate for the disadvantage of lower ordering degree in the structure, and the lower ordering of the FePt(BN, Re, C) film may be better understood from growth disorientation and defects in between interfaces. Therefore, this study provides the segregant design result for HAMR using FePt media with granular and columnar grains, showing that the 5d heavy transition metal can be used to replace the Ag segregant.

Author Contributions: J.-L.T. supervised, acquired funding, provided the conceptualization and methodology and design of the experiments, analyzed the data, and wrote and edited the paper; C.-Y.S. and J.-H.L. performed the sample preparation by sputtering and SQUID magnetic measurement; H.-T.T., C.-Y.S. and J.-H.L. performed the TEM microstructure and AFM surface investigation; C.-Y.S. and J.-H.L. fitted the data and plotted the figures. Y.-Y.H. provided the ideas and comments about the thin-film process equipment. All authors have read and agreed to the published version of the manuscript.

Funding: This research was funded by the Ministry of Science and Technology, Taiwan, grant number [MOST 111-2221-E-005-061]; Solar Applied Materials Technology Corp., Taiwan, grant number [110D610].

Acknowledgments: The authors would like to thank Solar Applied Materials Technology Corp. for sputtering target support.

Conflicts of Interest: The authors declare no conflict of interest. The founding sponsors had no role in the design of the study; in the collection, analyses, or interpretation of data; in the writing of the manuscript, and in the decision to publish the results.

References

1. Hono, K.; Takahashi, Y.K. L10 FePt Granular Films for Heat-Assisted Magnetic Recording Media. In *Ultrahigh Density Magnetic Recording*; Varvaro, G., Casoli, F., Eds.; Pan Stanford Publishing: Singapore, 2016; pp. 246–277.
2. Weller, D.; Parker, G.; Mosendz, O.; Lyberatos, A.; Mitin, D.; Safonova, N.Y.; Albrecht, M. Review Article: FePt heat-assisted magnetic recording media. *J. Vac. Sci. Technol. B* **2016**, *34*, 060801. [[CrossRef](#)]
3. Weller, D.; Mosendz, O.; Parker, G.; Pisana, S.; Santos, T.S. L10 FePtX–Y media for heat-assisted magnetic recording. *Phys. Status Solidi A* **2013**, *210*, 1245–1260. [[CrossRef](#)]
4. Futamoto, M.; Ohtake, M. Development of Media Nanostructure for Perpendicular Magnetic Recording. *J. Magn. Soc. Jpn.* **2017**, *41*, 108–126. [[CrossRef](#)]
5. Xu, C.; Zhou, B.; Du, T.; Varaprasad, B.S.D.C.S.; Laughlin, D.E.; Zhu, J. Understanding the growth of high-aspect-ratio grains in granular L10-FePt thin-film magnetic media. *APL Mater.* **2022**, *10*, 051105. [[CrossRef](#)]
6. Zhou, B.; Laughlin, D.E.; Zhu, J.G. The utilization of boron nitride (BN) for granular L10-FePt HAMR media fabrication. *Appl. Phys. Letter.* **2021**, *118*, 162403. [[CrossRef](#)]
7. Ju, G.P.; Peng, Y.G.; Chang, E.K.C.; Ding, Y.; Wu, A.Q.; Zhu, X.; Kubota, Y.; Klemmer, T.J.; Amini, H.; Gao, L.; et al. High-Density Heat-Assisted Magnetic Recording Media and Advanced Characterization—Progress and Challenges. *IEEE Trans. Magn.* **2015**, *51*, 3201709. [[CrossRef](#)]
8. Chen, S.; Xie, Q.; Zhou, C.; Zhou, J.; Deng, J.; Guo, R.; Peng, Y.G.; Ju, G.; Chen, J.S. Structure, magnetic and thermal properties of FePt-C-BN granular films for heat assisted magnetic recording. *J. Phys. D* **2020**, *53*, 135002. [[CrossRef](#)]
9. Platt, C.L.; Wierman, K.W.; Svedberg, E.B.; Van de Veerdonk, R.; Howard, J.K.; Roy, A.G.; Laughlin, D.E. L–1 0 ordering and microstructure of FePt thin films with Cu, Ag, and Au additive. *J. Appl. Phys.* **2002**, *92*, 6104–6109. [[CrossRef](#)]
10. Gilbert, D.A.; Wang, L.W.; Klemmer, T.J.; Thiele, J.U.; Lai, C.H.; Liu, K. Tuning magnetic anisotropy in (001) oriented L10 (Fe₁₂xCu_x)₅₅Pt₄₅ films. *Appl. Phys. Lett.* **2013**, *102*, 132406. [[CrossRef](#)]
11. Zhang, L.; Takahashi, Y.K.; Perumal, A.; Hono, K. L10-ordered high-coercivity (FePt)Ag–C granular thin films for perpendicular recording. *J. Magn. Magn. Mater.* **2010**, *322*, 2658–2664. [[CrossRef](#)]
12. Deng, J.Y.; Dong, K.F.; Peng, Y.G.; Ju, G.P.; Hu, J.F.; Chow, G.M.; Chen, J.S. Effect of TiON–MgO intermediate layer on microstructure and magnetic properties of L10 FePt–C–SiO₂ films. *J. Magn. Magn. Mater.* **2016**, *417*, 203–207. [[CrossRef](#)]
13. Tsai, J.L.; Li, H.K.; Pan, Z.Y.; Chang, Y.S.; Chen, Y.R.; Pi, C.; Wu, Y.T.; Chang, C.W. Magnetic Properties and Microstructure of FePt Films with MgTiON Intermediate Layer. *IEEE Trans. Magn.* **2017**, *53*, 8108404. [[CrossRef](#)]
14. Tsai, J.L.; Tzeng, J.L.; Hu, K.C.; Li, H.K.; Pan, Z.Y.; Chang, Y.S.; Liao, C.C. Microstructure and magnetic properties of FePt film with combined MoC/(Mg–X)O (X = Cu, Ni, Co) intermediate layers. *J. Magn. Magn. Mater.* **2017**, *422*, 262–270. [[CrossRef](#)]
15. Sepehri-Amin, H.; Nagano, M.; Seki, T.; Ho, H.; Tripathy, D.; Pirzada, S.; Srinivasan, K.; Yuan, H.; Dorsey, P.; Ajan, A.; et al. Microstructure and magnetic properties of FePt–(C, SiO₂) granular films deposited on MgO, MgTiO, and MgTiON underlayers. *Scr. Mater.* **2018**, *157*, 1–5. [[CrossRef](#)]
16. Hung, S.H.; McKenna, K. First-principles prediction of the morphology of L10 FePt nanoparticles supported on Mg(Ti)O for heat-assisted magnetic recording applications. *Phys. Rev. Mater.* **2017**, *1*, 024405. [[CrossRef](#)]
17. Chen, J.S.; Lim, B.C.; Ding, Y.F.; Chow, G.M. Low-temperature deposition of L10 FePt films for ultra-high density magnetic recording. *J. Magn. Magn. Mater.* **2006**, *303*, 309–317. [[CrossRef](#)]
18. Li, H.H.; Hu, J.F.; Ju, G.; Chow, G.M.; Chen, J.S. Effects of CrRu–SiO_x underlayer with MgO intermediate layer on the microstructure and magnetic properties of FePt–C thin film. *J. Appl. Phys.* **2011**, *109*, 07A736. [[CrossRef](#)]
19. Tsai, J.L.; Weng, S.M.; Dai, C.; Chen, J.Y.; Huang, L.C.; Hsu, T.W. Surface modification of FePt(Ag, C) granular film by ultrathin B₄C capping layer. *Appl. Surf. Sci.* **2020**, *509*, 145337. [[CrossRef](#)]
20. Yu, D.; Zhou, X.; Zhang, T.; Zhong, H.; Fu, Y.; Cui, W.; Wang, Q. Effects of B₄C Addition on the Microstructure and Magnetic Properties of FePt–C Granular Thin Films for Perpendicular Magnetic Recording. *IEEE Trans. Magn.* **2017**, *53*, 2300505. [[CrossRef](#)]
21. Gbadamasi, S.; Mohiuddin, M.; Krishnamurthi, V.; Verma, R.; Khan, M.W.; Pathak, S.; Kalantar-Zadeh, K.; Mahmood, N. Interface chemistry of two-dimensional heterostructures—fundamentals to applications. *Chem. Soc. Rev.* **2021**, *50*, 4684. [[CrossRef](#)] [[PubMed](#)]
22. Kadyrzhanov, K.K.; Shlimas, D.I.; Kozlovskiy, A.L.; Zdorovets, M.V. Research of the shielding effect and radiation resistance of composite CuBi₂O₄ films as well as their practical applications. *J. Mater. Sci. Mater. Electron.* **2020**, *31*, 11729–11740. [[CrossRef](#)]
23. Sharko, S.A.; Serokurova, A.I.; Novitskii, N.N.; Ketsko, V.A.; Smirnova, M.N.; Almuqrin, A.H.; Sayyed, M.I.; Trukhanov, S.V.; Trukhanov, A.V. A new approach to the formation of nanosized gold and beryllium films by ion-beam sputtering deposition. *Nanomaterials* **2022**, *12*, 470. [[CrossRef](#)] [[PubMed](#)]
24. Kozlovskiy, A.L.; Zdorovets, M.V. Synthesis, structural, strength and corrosion properties of thin films of the type CuX (X = Bi, Mg, Ni). *J. Mater. Sci.: Mater. Electron.* **2019**, *30*, 11819–11832. [[CrossRef](#)]
25. Zubar, T.I.; Usovich, T.I.; Tishkevich, D.I.; Kanafyev, O.D.; Fedkin, V.A.; Kotelnikova, A.N.; Panasyuk, M.I.; Kurochka, A.S.; Nuriev, A.V.; Idris, A.M.; et al. Features of galvanostatic electrodeposition of NiFe films with composition gradient: Influence of substrate characteristics. *Nanomaterials* **2022**, *12*, 2926. [[CrossRef](#)] [[PubMed](#)]
26. Kikuchi, N.; Kitakami, O.; Okamoto, S.; Shimada, Y.; Sakuma, A.; Otani, Y.; Fukamichi, K. Influence of 5d transition elements on the magnetocrystalline anisotropy of hcp-Co. *J. Phys. Condens. Matter.* **1999**, *11*, L485–L490. [[CrossRef](#)]

27. Pisana, S.; Mosendz, O.; Parker, G.J.; Reiner, J.W.; Santos, T.S.; McCallum, A.T.; Richter, H.J.; Weller, D. Effects of grain microstructure on magnetic properties in FePtAg-C media for heat assisted magnetic recording. *J. Appl. Phys.* **2013**, *113*, 043910. [[CrossRef](#)]
28. Nemoto, H.; Takekuma, I.; Nakagawa, H.; Ichihara, T.; Araki, R.; Hosoe, Y. Designing magnetics of capped perpendicular media with minor-loop analysis. *J. Magn. Magn. Mater.* **2008**, *320*, 3144. [[CrossRef](#)]
29. Yang, E.; Laughlin, D.E.; Zhu, J.G. Correction of order parameter calculations for FePt perpendicular thin films. *IEEE Trans. Magn.* **2012**, *48*, 7–12. [[CrossRef](#)]
30. Granz, S.D.; Kryder, M.H. Granular L10 FePt (001) thin films for heat assisted magnetic recording. *J. Magn. Magn. Mater.* **2012**, *324*, 287–294. [[CrossRef](#)]
31. Inoue, K.; Shima, H.; Fujita, A.; Ishida, K.; Oikawa, K.; Fukamichi, K. Temperature dependence of magnetocrystalline anisotropy constants in the single variant state of L10-type FePt bulk single crystal. *Appl. Phys. Lett.* **2006**, *88*, 102503. [[CrossRef](#)]
32. Richter, H.J.; Hellwig, O.; Florez, S.; Brombacher, C.; Albrecht, M. Anisotropy measurements of FePt thin films. *J. Appl. Phys.* **2011**, *109*, 07B713. [[CrossRef](#)]
33. Tsai, J.L.; Tseng, Y.T.; Li, C.R.; Fu, S.C. Magnetization reversal process in Fe/FePt films. *Appl. Phys. Lett.* **2010**, *96*, 032505. [[CrossRef](#)]
34. Tsai, J.L.; Weng, S.M.; Dai, C.; Chen, J.Y.; Lu, X.C.; Hsu, T.W. Temperature Dependence and Microstructure Effects on Magnetic Properties of FePt(B, Ag, C) Film. *Nanomaterials*. **2021**, *11*, 419. [[CrossRef](#)]
35. Trukhanov, S.V.; Trukhanov, A.V.; Vasiliev, A.N.; Balagurov, A.M.; Szymczak, H. Magnetic state of the structural separated anion-deficient $\text{La}_{0.70}\text{Sr}_{0.30}\text{MnO}_{2.85}$ manganite. *J. Exp. Theor. Phys.* **2011**, *113*, 819–825. [[CrossRef](#)]
36. Kozlovskiy, A.; Egizbek, K.; Zdorovets, M.V.; Ibragimova, M.; Shumskaya, A.; Rogachev, A.A.; Ignatovich, Z.V.; Kadyrzhanov, K. Evaluation of the efficiency of detection and capture of manganese in aqueous solutions of FeCeOx nanocomposites doped with Nb_2O_5 . *Sensors* **2020**, *20*, 4851. [[CrossRef](#)] [[PubMed](#)]
37. Yang, J.; Hou, W.; Pan, R.; Zhou, M.; Zhang, S.; Zhang, Y. The interfacial electronic engineering in polyhedral MOF derived Co-doped NiSe₂ composite for upgrading rate and longevity performance of aqueous energy storage. *J. Alloys Compd.* **2022**, *897*, 163187. [[CrossRef](#)]
38. Krishna, M.G.; Bhattacharya, A.K. Growth of rhenium oxide thin films. *Solid State Commun.* **2000**, *116*, 637–641. [[CrossRef](#)]
39. Ho, H.; Zhu, J.; Kulovits, A.; Laughlin, D.E.; Zhu, J.G. Quantitative transmission electron microscopy analysis of multi-variant grains in present L10-FePt based heat assisted magnetic recording media. *J. Appl. Phys.* **2014**, *116*, 193510. [[CrossRef](#)]
40. Varaprasad, B.S.D.C.S.; Takahashi, Y.K.; Wang, J.; Ina, T.; Nakamura, T.; Ueno, W.; Nitta, K.; Uruga, T.; Hono, K. Mechanism of coercivity enhancement by Ag addition in FePt-C granular films for heat assisted magnetic recording media. *Appl. Phys. Lett.* **2014**, *104*, 222403. [[CrossRef](#)]

Disclaimer/Publisher's Note: The statements, opinions and data contained in all publications are solely those of the individual author(s) and contributor(s) and not of MDPI and/or the editor(s). MDPI and/or the editor(s) disclaim responsibility for any injury to people or property resulting from any ideas, methods, instructions or products referred to in the content.